ORIGINAL ARTICLE

Large-scale process optimization for focused ion beam 3-D nanofabrication

**Ruwen Qin · Jing Fu · Zhaozheng Yin ·
Changxi Zheng**

Abstract With the ever-decreasing size of manufactured objects, fabrication processes driven by charged particle beams, such as focused ion beam (FIB), become important for a wide spectrum of interdisciplinary applications. A designed three-dimensional (3-D) pattern to fabricate may contain millions of pixels, which will require solving an unprecedented large-scale problem for planning. This paper proposes a general framework of planning FIB milling for fabricating 3-D nanostructures, including model formulations to enable FIB for scalable and automated applications and a corresponding optimization model to support the process planning. The implementation of proposed work does not affect the fabrication quality and yet tremendously reduces the required computational time and data storage during planning. The proposed framework of process planning is further illustrated and verified by simulation and milling experiments of submicron features on Si and Si_3N_4. This research offers an accurate and economical solution to the realization from designs to actual micro/nanoscale models and builds a scientific foundation for immediate development of complex, yet more accurate and cost-effective, beam scanning techniques.

Keywords Nanomanufacturing · Focused ion beam · Process planning · Large-scale optimization · Quadratic programming

R. Qin (✉)
Department of Engineering Management and Systems Engineering, Missouri University of Science and Technology (formerly University of Missouri-Rolla), Rolla, MO 65409, USA
e-mail: qinr@mst.edu

J. Fu
Department of Mechanical and Aerospace Engineering, Monash University, Clayton, 3800, Australia
e-mail: jing.fu@monansh.edu

Z. Yin
Computer Science Department, Missouri University of Science and Technology (formerly University of Missouri-Rolla), Rolla, MO 65409, USA
e-mail: yinz@mst.edu

C. Zheng
School of Physics, Monash University, Clayton, 3800, Australia

1 Introduction

Miniaturization has become an important theme in manufacturing with products in micro/nanoscale, bringing great impact to different industries as well as the society [1–4]. Various fabrication approaches have been developed, and the dimensions of artifacts manufactured today can be in the order of nanometer, which is equal to one-billionth of a meter. The definition of nanomanufacturing is broad in some sense and can be referred to as processes to fabricate objects or systems at the nanometer scale. To achieve the expected dimensions, fabrication processes are mainly driven by particle–solid interactions based on pixel scanning. The corresponding systems, including focused ion beam (FIB), focused electron beam, and alternatives with similar functionality, become standard tools for nanomanufacturing with capabilities of both additive ("bottom up") and subtractive ("top down") processes [5].

A comparison of macroscale and micro/nanoscale machining is presented in Fig. 1a. At macroscale, tool

Fig. 1 **a** Comparison of the three stages of machining at different scales, **b** test submicron spherical cavities milled on GaAs substrate with FIB, and **c** an example of scanning pattern with sparse pixels
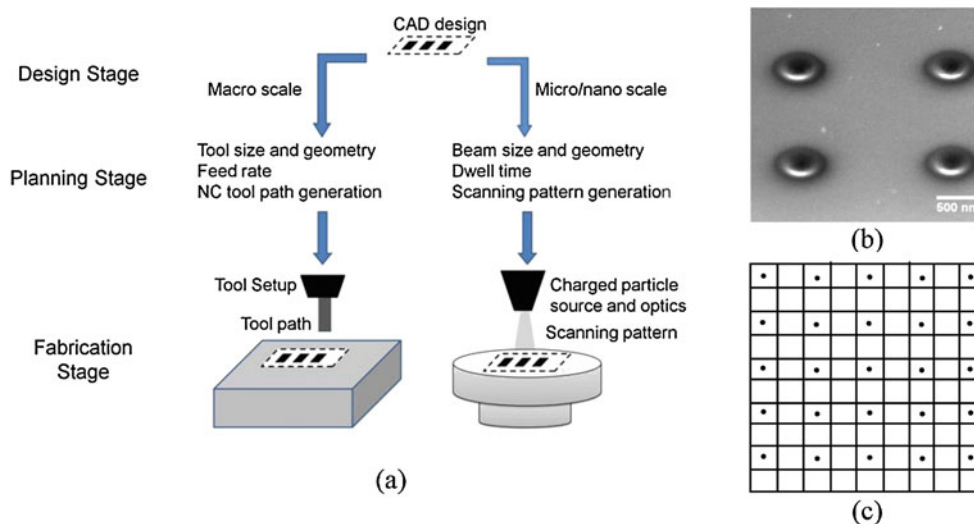
selection and numerical control patch can be translated and optimized for downstream machining processes [6, 7] or incorporated into the design stage [8]. Compared to well-studied design-to-manufacturing at macroscale, both the underlying physics and the associated planning techniques at micro/nanoscale are significantly different. Charged particle beams, instead of cutting tools, are often applied to "cut" the target material, and the effective pixel size of beam scanning in the highest resolution model is about 1 nm in current instruments. This allows for the realization of micro/nanoscale designs with high level of accuracy. Figure 1b displays submicron spherical cavities milled on GaAs substrate with FIB. Current charged particle-based systems can raster scan more than 10^5 pixels per second. Dwell time at each pixel, together with the beam sizes, can be determined and executed to directly translate three-dimensional (3-D) results from CAD designs. However, unlike automation at macroscale, limited planning tools are currently available to support 3-D freeform fabrication, even for simple geometries. A significant amount of trial-and-error efforts are often needed in current fabrication practices.

The aim of this study is to investigate the planning scheme for FIB milling processes, particularly for creating submicron features. Nanoscale milling with FIB involves the use of ion-sputtering technique to fabricate arbitrary 3-D objects [3, 4, 9–14]. The focused ions on material are of a near-Gaussian shape; therefore, the creation of a predetermined 3-D shape relies on the mathematical modeling of the spatial distribution of beam intensity and combined beam deflections [3, 4, 15–17]. Two representative approaches of 3-D FIB milling have been studied in the literature. One approach dedicates to the use of variable dwell time

to create desired 3-D shapes (e.g., [18]). The other approach using uniform dwell time produces a series of 2-D slices to form 3-D shapes (e.g., [19]). The work of this paper shares some similarity with the first approach in that dwell time is considered as a decision variable. The existence of various fabrication parameters dramatically increases the complexity of process planning for producing 3-D freeform structures, indicating the need for optimization tools to build a systematic planning framework for various applications based on FIB milling [2, 4]. An attempt to optimize FIB milling processes was presented in [20]. However, it was limited to one specific application, and no actual modeling or optimization framework was developed to extend the results to additional models. Little work has been done to study the process planning for FIB milling in a model-based optimization approach, and this research is the first attempt to explore that direction, which will serve as a standard computational approach for large-scale freeform fabrications. Results from optimized planning are expected to improve the cost-effectiveness and accuracy of beam scanning processes and to enhance the feedback cycle of micro/nanoscale products as well.

This paper formulates the process planning for FIB milling as a quadratic programming problem that permits varied dwell time at arbitrary beam settings. It supports implementation of the sparse scanning strategy we propose in this paper, as the solution of a linear system $\mathbf{At} = \mathbf{b}$ becomes more difficult to solve than in [18]. An FIB system typically has multiple current settings, similar to the selection of multiple tools in macroscale milling. Each setting is determined by the ion optics and corresponds to a fixed beam size. At focused mode, the spatial beam intensity distribution

can be modeled as a spatial Gaussian distribution, with the full width at half maximum of the distribution as the beam diameter. Scanning with a larger size beam on a single pixel will generate a cavity spanning more neighboring areas. Currently, a designed pattern to scan may include millions of pixels and, consequently, to determine the dwell time at each individual pixel becomes a large-scale nonlinear problem, often infeasible to solve in a reasonable time frame. One alternative approach is to divide the target geometry to multiple primitive features such as horizontal slices, which can then be programmed in a sequential manner [19]. However, this approach and other proposed methods intend to solve the dwell time only, with all the other decision variables such as beam current and spacing presumably provided by experts. The dimension of solvable patterns was supposed to be much larger than pixel size, and planning submicron and micron features is still challenging.

By investigating FIB process parameters, we propose a general framework of modeling and optimization for FIB milling in 3-D freeform fabrication. A sparse setup of the pixels to scan, referred to as sparse scanning and illustrated by Fig. 1c, is planned in the form of quadratic programming problem. Methods to improve the computational efficiency are also proposed to prepare for large-scale planning. Verifications are performed based on both simulation and milling experiments of submicron features, showing that the proposed approach can be further extended to features of varied size and geometry. The remaining of the paper is organized as follows: in Section 2, the planning of FIB milling is modeled as a quadratic programming problem. Section 3 discusses the solution approach to large-scale problems. Simulation studies are presented in Section 4 to develop a better understanding of the proposed planning approach, and Section 5 shows results from actual experiments. Findings from this study and discussions of potential future research are summarized in Section 6.

2 The optimization model

2.1 Formulation of sparse scanning for FIB milling

Without loss of generality, the planning of FIB process for producing designed 3-D shapes is assumed in a 3-D Euclidean space. A grid on the XY surface is set up with u columns on the X direction and v rows on the Y direction, as shown in Fig. 2. Therefore, there are N pixels in total, $N = u \times v$. Assume that the pixel size is δ nm on both X and Y directions. The operation of an FIB is to focus and deflect the beam on the XY grid. The geometry profile, $\mathbf{z}^O$ (in nanometers), is an $N \times 1$
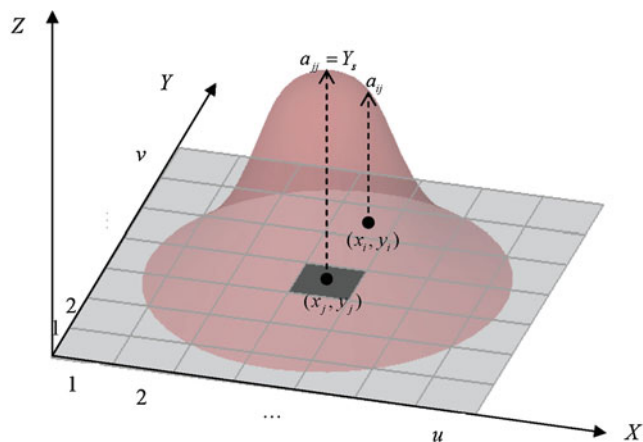

Fig. 2 A grid of pixels on the XY surface and the spatial Gaussian distribution of beam intensity centered at a scanned pixel (x_j, y_j)

vector specifying the desired depth on the Z direction for each of the N individual pixels.

The spacing of scanning, on both X and Y directions, is allowed to vary with current settings; however, the pixel size is kept unchanged. This approach allows the use of multiple current settings in producing a single shape yet without changing the standard of quality control (i.e., the total number of quality checkpoints is fixed). Assume only M pixels among N ($M \leq N$) are considered for milling (so named fabricated pixels). Therefore, the number of decision variables is reduced from N to M. The sparse level of scanning depends on the spacing of scanning and is measured by $1 - M/N$. For example, M is equal to N if every pixel will be considered for milling, and thereby the sparse level is 0 %. Approximately 25 % of pixels are considered for milling if the spacing of scanning is two pixels, yielding a 75 % sparse level of scanning.

Given any beam size, FIB process planning involves determining the dwell time on each of the fabricated pixels. Let $\mathbf{t}$ be an $M \times 1$ vector of which the jth element, t_j, represents the dwell time on the jth fabricated pixel, $j \in \{1, 2, \ldots, M\}$. The energetic collision at pixel j produces a cavity of a bell-shaped spatial geometry which spans over the neighboring pixels, as illustrated in Fig. 2. The shape can be described by the beam intensity function, typically modeled as a spatial Gaussian distribution [3]. Therefore, positive dwell time at the jth fabricated pixel affects the neighboring pixels and vice versa. $\mathbf{A}$, an $N \times M$ matrix, is set up to measure milling coefficients. As it is shown in Fig. 2, the element $a_{ij}(\geq 0)$ of $\mathbf{A}$ represents the yielded depth on the ith pixel contributed by the milling on the jth fabricated pixel with one unit of dwell time (i.e., 1 s). a_{ij} (in nanometers per second) at any current setting

can be decided by a near-Gaussian spatial distribution; therefore,

$$a_{ij} = Y_s \exp\left[-\frac{(x_i - x_j)^2 + (y_i - y_j)^2}{2\sigma_s^2}\right]. \qquad (1)$$

where (x_i, y_i) and (x_j, y_j) are the coordinates of the pixels i and j on the grid, respectively. σ_s (in nanometers) is the standard deviation of the spatial Gaussian distribution of beam intensity, and Y_s measures the speed of erosion (in nanometers per second), both at the current setting, s. The ultimate depth at pixel i is the aggregate results from milling on all the fabricated pixels [2]; that is,

$$z_i = \sum_{j=1}^{M} a_{ij} t_j = \mathbf{A}_i \mathbf{t}, \quad \text{for} \quad i = 1, 2, \ldots, N, \qquad (2)$$

where $\mathbf{A}_i$ is the ith row of coefficient matrix $\mathbf{A}$. The length of $\mathbf{A}_i$ has been reduced from N to M because of the reduced number of decision variables.

2.2 Optimization model of dwell time

The decision on dwell times, $\mathbf{t}$, must take two issues into consideration. The first issue is fabrication quality. It is desirable to make the material removal, $\mathbf{At}$, close to the geometry profile, $\mathbf{z}^O$, as much as possible. The other issue is the processing time cost. It is economical to keep the total dwelling time, $\mathbf{1}^T\mathbf{t}$, as minimum as possible. Consequently, a quadratic optimization problem is set up to take into account of both criteria,

$$\min F(\mathbf{t}) = \left\|\mathbf{At} - \mathbf{z}^O\right\|_2^2 + \eta \mathbf{1}^T \mathbf{t}$$
$$\text{subject to}: \quad \mathbf{t} \geq \mathbf{0} \qquad (3)$$

Equation 3 is also named the convex relaxation technique [21], which overcomes problems caused by an ill-conditioned, or even singular, matrix $\mathbf{A}$ in solving a linear system $\mathbf{At} = \mathbf{z}^O$. Therefore, Eq. 3 is more adaptive to a broader range of fabrication conditions and strategies. η (≥ 0) in Eq. 3 is the weight put on the processing time cost; therefore, it manages the tradeoff between fabrication quality and processing time cost. The objective function in Eq. 3 is rewritten to adopt a standard quadratic programming format:

$$\min F(\mathbf{t}) = \mathbf{t}^T \mathbf{Q} \mathbf{t} + 2\mathbf{p}^T \mathbf{t} + r$$
$$\text{subject to}: \quad \mathbf{t} \geq \mathbf{0} \qquad (4)$$

where

$$\mathbf{Q} = \mathbf{A}^T \mathbf{A},$$
$$\mathbf{p} = -\mathbf{A}^T \mathbf{z}^O + 0.5\eta \mathbf{1},$$
$$r = (\mathbf{z}^O)^T \mathbf{z}^O. \qquad (5)$$

$\mathbf{Q}$ in Eq. 5 is positive definite (because $\mathbf{Q} = \mathbf{A}^T\mathbf{A}$ and the columns of $\mathbf{A}$ are linearly independent). $\mathbf{p}$ can have both positive and negative elements. Equation 5 indicates that the size of the optimization problem varies with the sparse level of scanning; however, the number of quality checkpoints, N, always remains unchanged.

3 Solution approach

3.1 Size reduction of optimization problem

Scanning of a designed pattern for FIB milling may include millions of pixels, making (Eq. 4) a large-scale optimization problem. For example, the maximum pixel sizes of DualBeam 3-D (FEI Company, USA) are $u = 4096$ and $v = 3072$. Therefore, the number of decision variable may be $N = u \times v \approx 12.6 \times 10^6$, and $\mathbf{A}$ is an $N \times N$ matrix with $N^2 = 1.6 \times 10^{14}$ elements. The required memory to load matrix $\mathbf{A}$ into a computer is 6.4×10^{14} bytes $= 640$ TB $= 6.4 \times 10^5$ GB (each double precision floating number consists of 4 bytes), which is far beyond today's computing technology. However, we can utilize the sparse property of the coefficient matrix $\mathbf{A}$ to tackle the large-scale problem since the geometric effect at any pixel on the grid of planning is primarily contributed by the milling at that pixel and its neighboring pixels. Therefore, $\mathbf{A}$ can be saved as a sparse matrix to enhance the capability of dealing with large-scale problems. To save $\mathbf{A}$ as a sparse matrix, nonzero elements in $\mathbf{A}$, together with their row and column indexes, must be identified. A "local window" centered at each pixel is defined to efficiently identify the neighboring fabricated pixels that can contribute to the production of depth at the central pixel, shown in Fig. 3. Clearly, the size of the window is dependent on the beam intensity distribution of selected current, σ_s. For any pixel on the grid, it is reasonable to exclude fabricated pixels that are outside of a circle of $3\sigma_s$ radius centered at that pixel. Therefore, the diameter of the window, in the unit of pixels, is

$$w = 2\left\lceil \frac{3\sigma_s}{\delta} \right\rceil + 1. \qquad (6)$$

When raster scan is used, a square window, which circulates the circle window, is easier to implement in terms of problem formulation and analysis. The width of the square window is equal to w defined in Eq. 6. Therefore, we assume the pixel centered in the local window is affected by milling at any of the w^2 pixels within the square window.

Pixels within a local window are just a small portion of all pixels on the grid. Therefore, the number
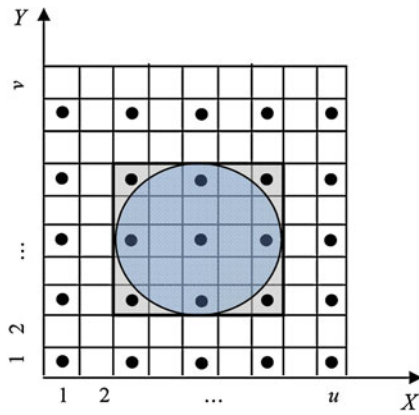
Fig. 3 A local window centered at a pixel determines the neighboring pixels whose milling effect to that pixel must be considered

of nonzero elements, $w^2 N$, is smaller than the total number of elements in matrix $\mathbf{A}$, N^2,

$$w^2 N \leq N^2. \tag{7}$$

However, the sparse level of matrix $\mathbf{A}$ may be severely decreased by the use of large-sized beams because w^2 increases with σ_s. The proposed sparse scanning has potential to prevent the quick increase in nonzero elements in matrix $\mathbf{A}$. When the beam size is increased, it is reasonable to enlarge the spacing of milling. Consequently, although more pixels are included by a larger local window, less pixels within that window will be actually milled. If fabricated pixels are evenly distributed on the grid, approximately $w^2 M$ elements of $\mathbf{A}$ are nonzero, and

$$w^2 M \leq w^2 N \leq N^2. \tag{8}$$

Therefore, matrix $\mathbf{A}$ may still be relatively sparse when larger beams are used.

3.2 An iterative approach of solution

The quadratic objective function in Eq. 4 is convex since $\mathbf{Q}$ is positive definite, and all decision variables are nonnegative. This type of problems is named nonnegative quadratic programming (NQP). No analytical solution for the global minimum of NQP exists and an iterative approach to solution (i.e., a gradient-based method) is commonly applied. Among the literature dedicated to NQP, multiplicative updates [22, 23] are perhaps the simplest algorithm to implement. It avoids the estimate of a learning rate that is commonly needed in gradient-based methods. Let $\mathbf{t}^0$ represent an initial value of $\mathbf{t}$, and $\mathbf{t}^k$ ($k > 0$) designates the result of $\mathbf{t}$ from the kth update. Multiplicative updates for searching an optimal solution to Eq. 4 are expressed as

$$t_j^{k+1} \leftarrow \frac{\max[-p_j, 0]}{(\mathbf{Qt}^k)_j} t_j^k. \tag{9}$$

Equation 9 means to use the jth (for $j = 1, 2, \ldots, M$) elements of vectors $\mathbf{Qt}^k$ and $\mathbf{P}$ to update the jth element of $\mathbf{t}^k$ in Eq. 9 is nonnegative since the numerator and denominator of that factor are both nonnegative. Therefore, solutions to Eq. 9 always remain in the feasible region for NQP during the iterative process. It is implied in Eq. 9 that the starting point of the iterative process, $\mathbf{t}^0$, must be positive. Otherwise, zero elements of $\mathbf{t}^0$ will remain unchanged throughout iterations.

The algorithm of updates in Eq. 9 will be derived in two steps. First, we will show that the updates in Eq. 9 monotonically decrease the objective function, $F(\mathbf{t})$. Then, we will prove that the updates in Eq. 9 converge to a global minimum, $F(\mathbf{t}^*)$, where $\mathbf{t}^*$ is the minimizer.

We define $G(\mathbf{s}, \mathbf{t})$ as a function of two positive vectors, $\mathbf{s}$ and $\mathbf{t}$:

$$G(\mathbf{s}, \mathbf{t}) = \mathbf{s}^T \mathbf{K(t)s} + 2\mathbf{p}^T \mathbf{s} + r, \tag{10}$$

where $\mathbf{p}$ and r have been defined in Eq. 5, and $\mathbf{K(t)}$ is a diagonal matrix with elements

$$K_{mn} = \begin{cases} (\mathbf{Qt})_m/t_m, & \text{if } m = n; \\ 0, & \text{otherwise.} \end{cases} \tag{11}$$

From Eq. 4, we have

$$G(\mathbf{t}, \mathbf{t}) = F(\mathbf{t}). \tag{12}$$

Moreover, $G(\mathbf{s}, \mathbf{t})$ is an upper bound of $F(\mathbf{s})$, that is

$$G(\mathbf{s}, \mathbf{t}) \geq F(\mathbf{s}), \tag{13}$$

which can be derived for all positive vectors $\mathbf{s}$ and $\mathbf{t}$ as follows. Since $G(\mathbf{s}, \mathbf{t}) - \mathbf{F}(\mathbf{s}) = \mathbf{s}^T(\mathbf{K(t)} - \mathbf{Q})\mathbf{s}$, to prove the inequality in Eq. 13 is equivalent to showing that $\mathbf{K(t)} - \mathbf{Q}$ is positive semidefinite. The Hadamard product of two positive vectors, $\mathbf{s}$ and $\mathbf{t}$, $\mathbf{s} \circ \mathbf{t}$, is still a positive vector, and

$$
\begin{aligned}
(\mathbf{s} \circ \mathbf{t})^T &(\mathbf{K(t)} - \mathbf{Q})(\mathbf{s} \circ \mathbf{t}) \\
&= \sum_{mn} s_m t_m (K_{mn} - Q_{mn}) t_n s_n \\
&= \sum_{mn} Q_{mn} t_m t_n s_m^2 - \sum_{mn} Q_{mn} t_m t_n s_m s_n \\
&= \frac{1}{2} \sum_{mn} Q_{mn} t_m t_n (s_m - s_n)^2 \\
&\geq 0.
\end{aligned}
\tag{14}
$$

$\mathbf{K}(\mathbf{t}) - \mathbf{Q}$ being positive semidefinite verifies that $G(\mathbf{s}, \mathbf{t})$ is an upper bound of $F(\mathbf{s})$. Therefore, $G(\mathbf{s}, \mathbf{t})$ is an auxiliary function for $F(\mathbf{t})$.

Because $\mathbf{Q}$ is positive definite, $\mathbf{K}(\mathbf{t})$ is positive definite as well according to Eq. 11. Therefore, $G(\mathbf{s}, \mathbf{t})$ is convex on $\mathbf{s}$. The choice of

$$\mathbf{s}' = \arg\min_{\mathbf{s}} G(\mathbf{s}, \mathbf{t}) \tag{15}$$

ensures that

$$F(\mathbf{s}') \le G(\mathbf{s}', \mathbf{t}) \le G(\mathbf{t}, \mathbf{t}) = F(\mathbf{t}); \tag{16}$$

and $F(\mathbf{s}') < F(\mathbf{t})$ if $\mathbf{s}' \ne \mathbf{t}$. We take the first derivative of G with respect to $\mathbf{s}$ to find that

$$\frac{\partial G(\mathbf{s}, \mathbf{t})}{\partial \mathbf{s}} = 2\mathbf{K}(\mathbf{t})\mathbf{s} + 2\mathbf{p}. \tag{17}$$

$\partial G(\mathbf{s}, \mathbf{t}) / \partial s_j > 0$ when $p_j \ge 0$; therefore, the solution to Eq. 15 is $s'_j = 0$ under this condition. There exists a solution to $\partial G(\mathbf{s}, \mathbf{t}) / \partial s_j = 0$ when $p_j < 0$, that is

$$s'_j = -\frac{p_j}{(\mathbf{Qt})_j} t_j. \tag{18}$$

Therefore, the solution to Eq. 15 at any value of p_j can be written as Eq. 9.

Next, we show that the fixed point of the updates in Eq. 9, $\mathbf{t}^*$, satisfies the Karush–Kuhn–Tucker (KKT) conditions [24] to the NQP problem defined in Eq. 4. The KKT conditions are as follows:

$$\mathbf{Qt} + \mathbf{p} = \lambda, \quad \mathbf{t} \ge \mathbf{0}, \quad \lambda \ge \mathbf{0}, \quad \mathbf{t} \circ \lambda = \mathbf{0}, \tag{19}$$

where λ is a vector whose elements are Lagrange multipliers that enforce the nonnegativity constraints on $\mathbf{t}$. "$\circ$" in Eq. 19 represents the Hadamard product. $\mathbf{t}^*$ satisfying the KKT conditions implies that either of the following two conditions must hold for each element of $\mathbf{t}^*$: (i) $t_j^* = 0$; or (ii) $\frac{\partial F}{\partial t_j}|_{\mathbf{t}^*} = 0$ if $t_j^* > 0$. Equation 9 shows that $\max[-p_j, 0] / (\mathbf{Qt}^*)_j = 1$ for $t_j^* > 0$. Under this condition, λ_j, which is equal to $\frac{1}{2}\frac{\partial F}{\partial t_j}|_{\mathbf{t}^*} = (\mathbf{Qt}^*)_j + p_j$, is 0. That is, the fixed point of the updates in Eq. 9 satisfies the KKT conditions of Eq. 4. Since $F(\mathbf{t})$ is strictly convex on $\mathbf{t} \ge \mathbf{0}$ and $\mathbf{t}_0$ is not the origin, the updates defined in Eq. 9 generate solutions $\{\mathbf{t}_0, \mathbf{t}_1, \mathbf{t}_2, \dots\}$ that makes the sequence $\{F(\mathbf{t}_0), F(\mathbf{t}_1), F(\mathbf{t}_2), \dots\}$ monotonically decrease and converge to the global minimum, $F(\mathbf{t}^*)$.

3.3 Processing time cost

The value of η represents the ratio of processing time cost relative to the cost pertaining to fabrication quality. It manages the tradeoff between these two costs.

To better understand the impact of η on the optimal solution to Eq. 4, $\mathbf{t}^*$, we rewrite Eq. 9 as follows:

$$t_j^{k+1} \leftarrow \frac{\max\left[\mathbf{A}_j \cdot \mathbf{z}^O - 0.5\eta, 0\right]}{\mathbf{A}_j \cdot (\mathbf{At})} t_j^k \tag{20}$$

to explicitly show η in the updates. "$\cdot$" in Eq. 20 represents the inner product of two vectors. $\mathbf{A}_j$ in Eq. 20 is the jth column of the coefficient matrix $\mathbf{A}$, which represents the yield of the jth fabricated pixel at all pixels of planning. $\mathbf{A}_j$, $\mathbf{z}^O$, $\mathbf{At}^*$, and all $\mathbf{At}^k$ are vectors in an N dimensional Euclidean space. $\mathbf{At}^*$ is close to $\mathbf{z}^O$, and the vector pointing from $\mathbf{At}^*$ to $\mathbf{z}^O$, $\mathbf{At}^* - \mathbf{z}^O$, is the minimized errors of FIB milling for the N pixels of planning. The updates in Eq. 20 involve searching $\mathbf{At}^*$, iteratively, and $\mathbf{At}^t - \mathbf{z}^O$ is the error associated with the result from the kth iteration. The path of search in the N dimensional space, $\{\mathbf{At}^1, \mathbf{At}^2, \dots\}$, is affected by η as the factor multiplying t_j^k is a function of η in Eq. 20.

Besides the path of search, the location of $\mathbf{At}^*$ on the N dimensional space is also affected by η. At $\mathbf{At}^*$, where the search is accomplished, the vector of minimized error, $\mathbf{At}^* - \mathbf{z}^O$, and t_j^* (for $\forall j$) satisfy

$$\begin{cases} \mathbf{A}_j \cdot (\mathbf{At}^* - \mathbf{z}^O) = -0.5\eta, & \text{if } 0 \le \eta < 2\mathbf{A}_j \cdot \mathbf{z}^O \\ t_j^* = 0, & \text{if } \eta \ge 2\mathbf{A}_j \cdot \mathbf{z}^O \end{cases} \tag{21}$$

In general, fabrication quality decreases with the increase in η. Under an extreme situation of $\eta = 0$, the error vector, $\mathbf{At}^* - \mathbf{z}^O$, is required to be equal to $\mathbf{0}$ or perpendicular to vector $\mathbf{A}_j$ for all j. Positive η relaxes the restriction on error. As η increases, some elements in $\mathbf{t}^*$ become zeros; others also no longer satisfy the perpendicular relationship between $\mathbf{At}^* - \mathbf{z}^O$ and $\mathbf{A}_j$, according to Eq. 21. If η keeps increasing, the other extreme situation will occur, ultimately; that is, all elements of $\mathbf{t}^*$ become zeros. This means no milling is the best solution to Eq. 4 when milling cost is tremendously high, which clearly is not appropriate for most real world applications. Very large η may fail the model in Eq. 4, and the NQP problem in Eq. 4 needs to be revised to adapt to situations that the processing time cost is dominating; for instance, minimizing the milling error subject to a budget constraint on processing time cost.

4 Numerical simulation

4.1 Numerical examples

A numerical example that uses 100 pA to mill a spherical lens governed by

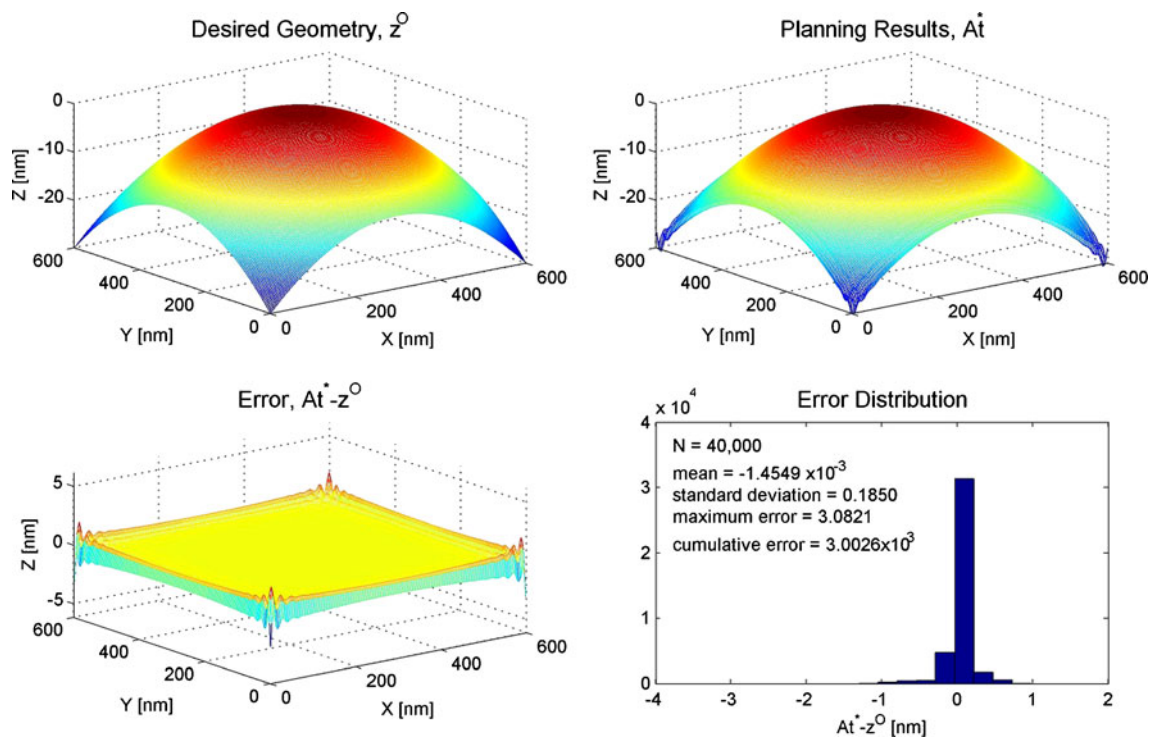$$z_i^O = R - \sqrt{R^2 - x_i^2 - y_i^2}, \quad |x_i| \le h_x, \quad |y_i| \le h_y \tag{22}$$

Fig. 4 Numerical results of the spherical lens example

is first studied. $h_x = h_y = 300$ nm, and the pixel size is 3 nm on both X and Y directions. Consequently, a 200 by 200 grid is set up, and the total number of pixels, N, is equal to 4×10^4. The beam diameter corresponding to this current setting is 23 nm. A silicon (Si) wafer sample is used, for which the sputtering rate is known
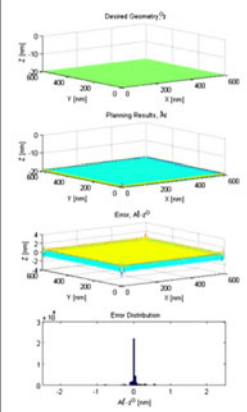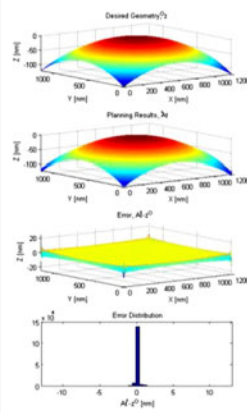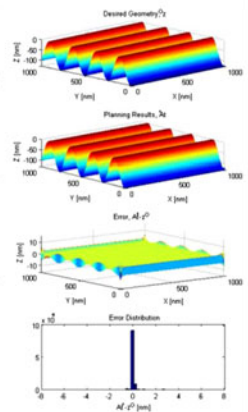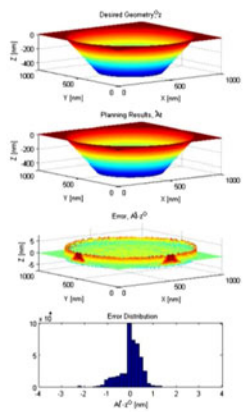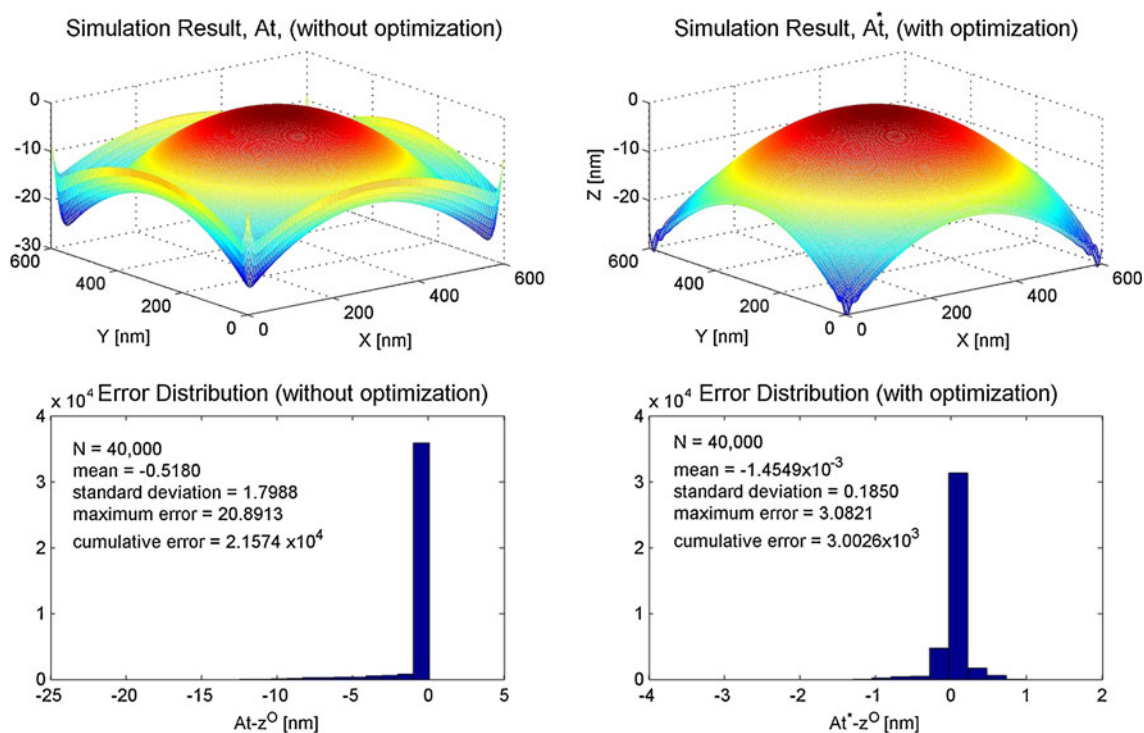

Fig. 5 Simulation results of the submicron spherical lens based on yield calculation only (without optimization) and the proposed optimization approach

(0.27 μm^3/nC). The volume of removal is 3,608,437 nm^3, and the spacing of scanning is 3 pixels. Consequently, the number of decision variables is just about 11 % of the 4×10^4 pixels under planning. We solve the problem using Matlab on a Dell desktop (OptiPlex 760: Intel(R) Core(TM)2 Duo CPU, 2.6 GHZ, and 4-Gb memory). The matrix **A** was generated in 0.9 s. The optimization process took 29.0 s when we set the termination condition as $||t^k - t^{k-1}||_1/M < 1$ ns or the number of iterations >500 (detailed information about the computational requirement is presented in Fig. 7).

Simulation results of this example are displayed in Fig. 4. The plot on the upper left is the desired 3-D shape with $R = 3$ μm. The plot on the upper right is the simulation result from the optimized FIB process planning with $\eta = 0$. The optimized planning result is very close to the desired 3-D shape. The difference between these (i.e., the error on the Z direction), $\mathbf{A}t^* - \mathbf{z}^O$, is displayed at the bottom left. Large errors mainly occur on the XY boundaries of the shape. The plot at the bottom right is the statistical distribution of the error. Mean value of the error on the 4×10^4 pixels is -1.4549×10^{-3} nm. The standard deviation of the error is 0.1850 nm. The 95 % confidence interval of the mean is $[-0.0033, 0.0004]$, indicating the mean value of errors is from a normal distribution centered at zero. The maximum absolute value of error, 3.0821 nm, occurs at a corner. The cumulative error on the Z direction is 3.0026×10^3 nm, equivalent to a 0.75 % deviation from the desired volume of removal. Total dwell time is 150.4 ms. The statistical results show that the deviation is limited by the proposed planning approach.

	square cavity	spherical lens	sinusoidal grating	pore on membrane
geometry profile	$z_i = -20$	$z_i = 3000 - \sqrt{3000^2 - (x_i^2 + y_i^2)}$	$z_i = 64 + 63\cos\left(-\dfrac{\pi}{8} + \dfrac{x_i}{256}\right)$	$z_i = \begin{cases} 500 & \sqrt{x_i^2 + y_i^2} \le 250 \\ 1000 - 2\sqrt{x_i^2 + y_i^2} & 250 < \sqrt{x_i^2 + y_i^2} \le 500 \\ 0 & \sqrt{x_i^2 + y_i^2} > 500 \end{cases}$
current	100 pA	100 pA	50 pA	50 pA
material	Si	Si	Si_3N_4	Si_3N_4
pixel size	3 nm	3 nm	3 nm	1.5 nm
# pixels	200x200	400x400	334x334	667x667
spacing	9 nm	9 nm	9 nm	9 nm
processing time	0.2835 s	2.2916 s	6.582 s	22.96 s
simulation results of planning				
statistical results of errors	N=40,000 mean=-1.4072x10⁻³ nm std=0.1677 nm max error=2.0061 nm cum error=2.9599x10³ nm relative error=0.37% nm	N=160,000 mean=-2.7460x10⁻³ nm std=0.4976 nm max error=12.258 nm cum error=2.4496x10⁴ nm relative error=0.38%	N=111,556 mean=-2.8293x10⁻³ nm std=0.5720 nm max error=7.7950 nm cum error=1.9545x10⁴ nm relative error=0.28%	N=444,889 mean=3.5265x10⁻² nm std=0.5853 nm max error=3.7939 nm cum error=1.7032x10⁵ nm relative error=0.17%
CPU time*	30 s	114 s	69 s	69 s

*Maximum number of iterations = 500

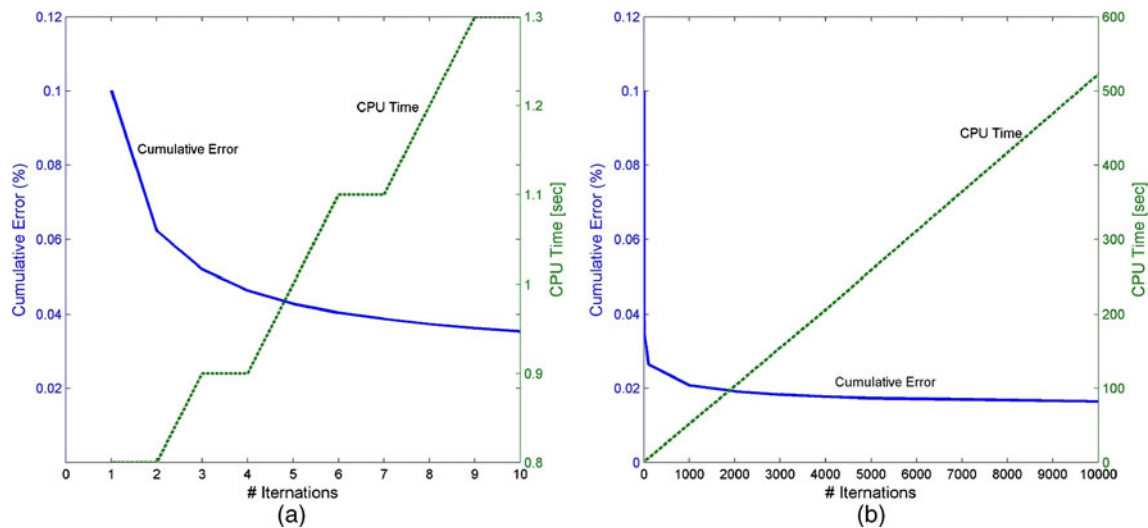**Fig. 6** Summary of numerical examples

Fig. 7 CPU time (in seconds) and cumulative error (in percentage) against the number of iterations, k, for the spherical lens example: **a** $k = 10$ and **b** $k = 10,000$

We compare the improvement by optimization in this example to a nonoptimization setting. The user manual of FIB instrument (FEI Company, USA) gives a method for estimating the dwell time [25]:

$$\mathbf{t} = \frac{10^{-9}(\delta[\text{nm}])^2}{(\text{current}[\text{nA}])(\text{sputtering rate}[\mu\text{m}^3/\text{nC}])} \mathbf{z}^O. \quad (23)$$

Planning results, which are based on yield calculation only (without optimization), is displayed on the left of Fig. 5, and our optimization results are on the right. Improved geometry fidelity is clearly accomplished by the proposed optimization, and the error statistics shown in Fig. 5 further confirms the improvement.

To understand the factors affecting the computational time for optimization, we perform several tests and summarize results in Fig. 6. For a square cavity with a uniform depth of 20 nm on the Z direction, with all else kept unchanged, the optimization time is 30 s. No significant change in the computational time has been observed from this comparison, which indicates that geometry complexity does not impact the CPU time of optimization. We further optimize the process plan for a spherical lens with a bigger size, on a 1.2 by 1.2-μm grid, and all other settings remain unchanged.

The size of the grid is four times of the original one, and the number of decision variables are also increased by four times. The computational time for optimizing the process plan is 114 s, approximately four times of the computational time for optimizing the smaller lens. The tests suggests that the computational time is not affected by geometry complexity but is dependent on problem sizes. Additional examples are also studied including a sinusoidal grating and a pore on membrane, and results from all the examples are consistent.

The efficiency of the proposed approach in Eq. 4 depends on the selection of termination condition. It will cost additional computational time if a solution of high accuracy is expected. Figure 7 displays the cumulative error in percentage, $\|\mathbf{A}\mathbf{t}^k - \mathbf{z}^O\|_1 / \|\mathbf{z}^O\|_1$, and corresponding computational time, both against the number of iterations, k. Figure 7a shows that the cumulative error decreases rapidly in the initial several iterations. Figure 7b further shows that the computational time linearly increases with the increase in iterations, and yet the decrease in cumulative error gradually slows down. The decision on when an approximate solution is of sufficiently high quality is case-dependent, and simple heuristics are often developed to facilitate the selections.

Setting (s)	Current [pA]	Beam diameter (d_s) [nm]	SD of intensity Dist (σ_s) [nm]	Current density [nA/μm]	Erosion rate (Y_s) [μm/s]
1	1	7	2.97	18.04	4.87
2	100	23	9.77	240.69	45.02
3	1000	50	21.23	509.30	95.34

Table 1 Current settings with the corresponding current density and erosion rate for 30 keV gallium ion milling on silicon
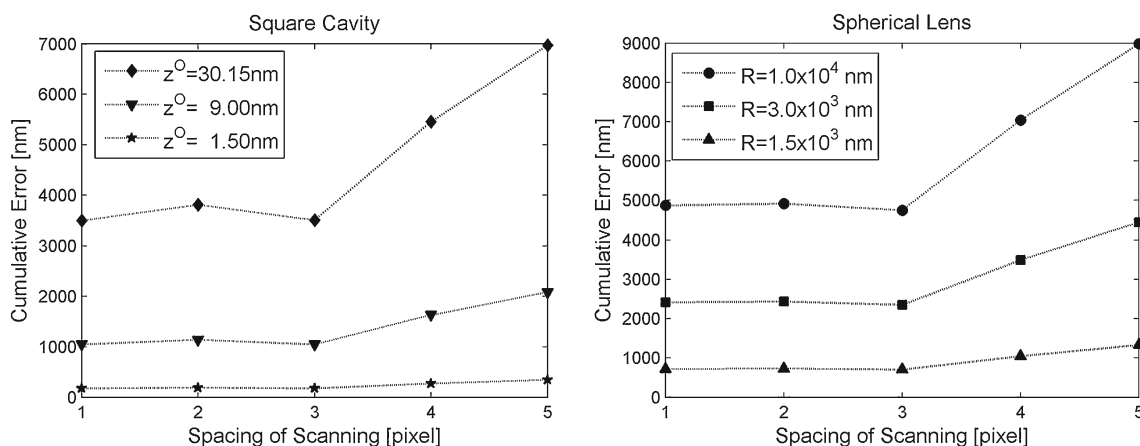
Fig. 8 Minimized cumulative error at the current 100 pA

4.2 Study design

The proposed framework in this paper formulates the dwell times as an optimization problem. To develop a scientific understanding of the model-based optimization approach to process planning, we examine the optimization result for varied fabrication settings. Factors that may influence the optimization result include the geometry complexity of 3-D objects, maximum depth of fabrication, size of focused ion beam, and spacing of scanning.

To determine if the geometry complexity affects the optimization outcome, two representative 3-D shapes are compared. The first one is the square cavity that has a uniform depth on the Z direction; whereas the other is the spherical lens that has a curved depth. Both are within a 600 by 600 nm area on the XY surface.

Three levels of maximum depth on the Z direction are selected for each shape to study the effect of milling depth. 1.5, 9, and 30 nm are selected for the square cavity. Three levels of R (1.5, 3, and 10 μm), corresponding to three different maximum depths on the Z direction, are selected for the spherical lens.

Three current settings, 1, 100, and 1,000 pA, are displayed in Table 1. The current density can be calculated for each current setting, s, according to Eq. 1. Given the characteristics of the bombarding ion and

the target material, erosion rate, Y_s, is considered as a constant in this study. It can be obtained by multiplying the maximum current density with ion-sputtering rate. For example, for 30 keV gallium ion milling on Si, the sputtering rate is 0.27 μm^3/nC at normal incidence [26]. It should be noted that the sputtering rate may decrease with the increase in aspect ratio due to the redeposition effect. It may also increase if the dwell time of a single deflection on a pixel is too long.

The optimization of process planning is expected to be effective if the spacing of FIB scanning is limited below a threshold. This is because positive overlap of beam scanning (i.e., scanning spacing is less than the beam diameter) is needed to avoid the situation that some areas are left, not fabricated. Therefore, identification of the threshold is critical. The threshold spacing of FIB scanning is the largest spacing (or the smallest overlap) that does not sacrifice fabrication quality. The optimization model makes it possible to identify the threshold because, with it, we can study how the minimized cumulative error is affected by the spacing of FIB scanning. Spacing no greater than 1.5σ is suggested in [3]; therefore, we consider spacing up to 1.5σ (i.e., from 1 to 5 pixels) in the examples.

Table 2 Mean and variance of minimized milling error at different spacing of FIB milling

Groups	Mean	Variance
Spacing = 1 pixel	−0.00082	0.019167
Spacing = 2 pixels	−0.00081	0.019021
Spacing = 3 pixels	−0.00079	0.018693
Spacing = 4 pixels	−0.00149	0.032984
Spacing = 5 pixels	−0.00280	0.062073

Table 3 Significant levels for t test and F test

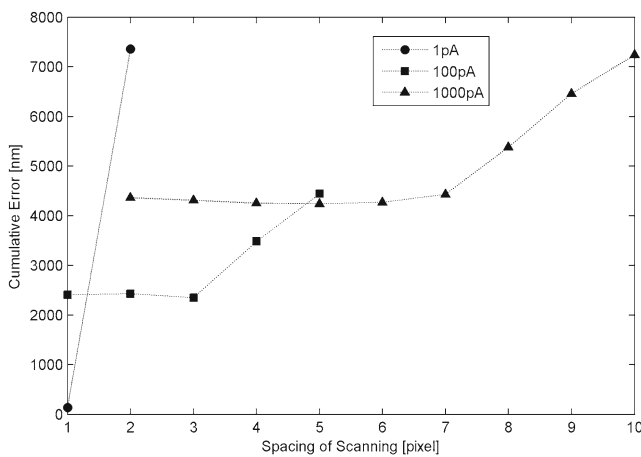|	1 pixel	2 pixels	3 pixels	4 pixels	5 pixels
1 pixel		0.996	0.981	0.556	0.164
		0.446	0.124	0.000	0.000
2 pixels			0.985	0.553	0.163
			0.082	0.000	0.000
3 pixels				0.541	0.158
				0.000	0.000
4 pixels					0.395
					0.000

Fig. 9 Minimized cumulative errors against milling spacing at different current settings

4.3 Numerical results

Figure 8 displays the cumulative errors for both 3-D shapes at their three levels of maximum depth when the current is 100 pA. The results imply that the minimized cumulative error is relatively even when the spacing is not greater than 3 pixels, equivalent to a 61 % overlap (overlap=1−spacing/beam diameter). The same pattern is consistently observed for both shapes at all levels of maximum depth, which suggest that the shape and maximum depth of the 3-D nanostructure to fabricate have no significant impact on the optimization result. The impact of spacing on the minimized error is further examined from a statistical viewpoint. Table 2 lists the mean and variance of minimized error for the spherical lens when using the 100 pA ion current. Both the mean and variance of minimized error show a clear change as the spacing of scanning increases from 3 to 4 pixels (3 nm per pixel), which are verified by the t test and F test results in Table 3.

We also examine the threshold spacing for varied current settings. Figure 9 displays the minimized cumulative error at different spacings for the selected three current settings. At the 1- pA current, the spacing of

1 pixel effectively controls the milling error. When the current is increased from 1 pA to 100 pA, the spacing of scanning can be increased to 3 pixels without sacrificing the fabrication quality. At the 1,000-pA current, the spacing can be as large as 7 pixels. The threshold spacing (in the unit of σ), L^*, and overlap (in the unit of beam diameter), of scanning for the three current settings are further summarized in Table 4. In the table, it has been shown that the threshold spacing of FIB scanning is about 1σ or the threshold overlap is near 0.58, at any of the three current settings.

When larger current is used, enlarging the spacing of scanning from 1 pixel to the threshold level dramatically improves the computational efficiency without lowering fabrication quality. The improved computation efficiency is due to the reduced number of decision variables and the smaller size of the coefficient matrix **A**, as Table 4 summarizes. Without sparse scanning (i.e., every pixel is fabricated), the number of nonzero elements in each row of **A** (w^2) significantly increases as the beam diameter, d, increases. By implementing the sparse scanning, the number of nonzero elements in each row of **A**, $w^2 M/N$, remains at a lower level that makes it feasible for solving the optimization problem.

5 Milling experiments

The spherical lens defined in Eq. 22 is first used to verify the proposed planning approach. All the milling experiments were performed on DualBeam 3-D (FEI Company, USA) equipped with a liquid metal ion source of gallium. The simulation studies in Section 4 have suggested that optimal planning result can be affected by the beam current and spacing of FIB scanning. Therefore, we tested the proposed optimization method in two-factor (current × spacing) four-level full factorial experiments. Spacing is changed from 1 to 4 pixels (pixel size is 6 nm on both X and Y directions), and the current settings are 1, 30, 100, and 500 pA. There are 16 experiments in total, as shown in Table 5.

Table 4 The threshold spacing (and overlap) of FIB that provides satisfied milling quality and high computational efficiency

Current pA	Beam diameter (d) [nm]	Standard deviation of beam intensity distribution (σ) [nm]	Threshold spacing (L^*)		Threshold overlap ($1 - L^*/d$)	Sparse level ($1 - M/N$)	The number of nonzero elements in each row of **A**	
			[nm]	(σ)			at min spacing (w^2)	at optimal spacing ($w^2 M/N$)
1	7	2.97	3	1.01	0.57	0.000	49	49
100	23	9.77	9	0.92	0.61	0.889	441	49
1,000	50	21.23	21	0.99	0.58	0.980	2,025	41

Table 5 Optimization results of milling experiments

ID	Current	Spacing	Cumulative error by optimized planning	Planned total processing time (standard)	Volume of removal (theoretic value=5.815E-02 μm³)	
	[pA]	[pixel]	[nm]	[ms]	[μm³]	Error [%]
a	1	1	N/A	210,074.43	5.815E-02	−0.0025 %
b	1	2	1,027,231	117,814.74	3.254E-02	−44.0358 %
c	1	3	1,352,687	57,417.96	1.581E-02	−72.8064 %
d	1	4	1,466,396	32,922.76	9.024E-03	−84.4813 %
e	30	1	3,237	7,427.81	5.815E-02	−0.0041 %
f	30	2	12,364	7,408.27	5.814E-02	−0.0172 %
g	30	3	163,686	7,296.34	5.730E-02	−1.4680 %
h	30	4	533,400	6,409.54	4.966E-02	−14.5975 %
i	100	1	5,465	2,275.38	5.815E-02	−0.0068 %
j	100	2	7,499	2,272.38	5.815E-02	−0.0099 %
k	100	3	13,570	2,266.90	5.814E-02	−0.0178 %
l	100	4	101,026	2,261.89	5.779E-02	−0.6173 %
m	500	1	8,615	477.59	5.814E-02	−0.0097 %
n	500	2	8,643	477.58	5.814E-02	−0.0097 %
o	500	3	11,024	476.86	5.814E-02	−0.0129 %
p	500	4	15,633	474.40	5.814E-02	−0.0246 %

In each experiment, pixels to mill are determined by the scanning spacing for that experiment; then coefficient matrix, **A**, is generated for the given current. The optimization problem in Eq. 4 is solved to find the optimal dwell time for each selected pixel. Indexes of these pixels and the corresponding dwell time are saved as ASCII codes and sent to the FIB instrument through the "stream" interface provided by the manufacturer.

The maximum size of 4,096 by 3,072 for beam scanning is limited by the control unit of the instrument. To illustrate the entire implementation process, FIB milling is assumed to be on a grid, similar to that in the simulation study, and unless stated elsewhere, each grid pattern for test contains 200 by 200 pixels. At ×6,500 magnification, the pixel size is approximately 6 nm, and the corresponding spacing can be varied at $6q$ nm (q is a positive integer). A silicon wafer sample is mounted for milling, and the sputtering rate is 0.27 μm³/nC. The total volume for removal to produce the spherical lens (with $R = 3$ μm) is 0.05815 μm³, and the total milling time varies with current settings. In Table 5, we provide the simulation results for experiments, including the minimized cumulative error on the Z direction, total milling time, and realized volume of removal, all based on the optimized planning for FIB scanning.

The scanning electron microscope (SEM) images of the experiment results are presented in Fig. 10. Results in the same row are produced with the same current, and the same spacing of scanning is used for results in the same column. To achieve quality finish at the pixel size of 6 nm, the current should be large enough to

form a beam diameter no less than 14 nm (= 6 nm/(1 − 0.58)), or equivalently, a standard deviation of beam intensity distribution no less than 6 nm (since $\sigma \geq 6q$). For the results in the first row with the lowest current, 1 pA, the beam diameter is approximately 7 nm, and the standard derivation of beam intensity distribution
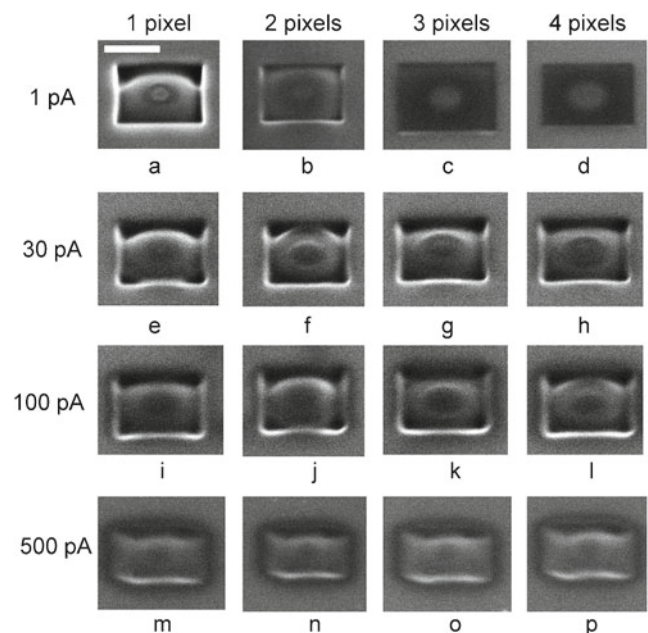

Fig. 10 SEM imaging (tilted at 45°) of FIB-milled patterns on Si with varied settings: **a–d** 1 pA, **e–h** 30 pA, **i–l** 100 pA, **m–p** 500 pA. (*scale bar* 500 nm)

is 2.97 nm, smaller than the minimum requirements of scanning spacing. The milled geometries, however, are still close to the expected one with 1- and 2-pixel spacing. It implies that the tail effect at this current setting may be larger than the Gaussian distribution model used by the process planning. For larger spacing, the yielded geometries (Fig. 10c–d) are significantly different from the designed geometry, which primarily are the results of insufficient overlap of beam scanning. At the 6-nm pixel size, 30 and 100-pA current settings (Fig. 10e–l) appear to be more appropriate compared to 1-pA current in terms of the fidelity of the geometries produced. Yet "roughened" surface can be observed by milling with larger beams, consistent with the results of simulation. It should be noted that 30 and 100 pA offer much higher milling rate (in cubic micrometers per second) compared to 1 pA. The milling time for the test pattern by 1 pA is more than 3 min, but only seconds by 30 and 100 pA. Results from the current setting of 500 pA (Fig. 10m–p) are not convincing. A possible reason is that the beam covers a large number of pixels within an extremely short time and, therefore, ion dose may not be properly delivered to each pixel.

Although threshold spacing for the current setting of 100 pA is suggested to be between 1.61 and 1.63 pixels, theoretically, experimental results show that the milling error does not increase significantly as the spacing of scanning is enlarged to 2 pixels and yet becomes sub-stantially large as the spacing is greater than 2 pixels. The current setting such as 500 pA used in the experiment may not be appropriate for small features due to large beam size and extremely short dwell time during scanning. Additional constraints can be enforced in the optimization model to prevent improper settings identified by experiments and, eventually, an automated design-to-fabrication scheme can be accomplished.

To further demonstrate the proposed approach, single submicron pores on membrane were milled as shown in Fig. 11a. Si window-coated Si_3N_4 membrane of 500 nm in thickness was chosen, with free standing membrane in the center of a 2 by 2-mm region. FIB milling commands (the X and Y indexes of pixels selected to mill and the dwell time on these pixels) then were transferred to the instrument, and no coating is performed prior to milling. To control the beam charging effect, electron beam was also scanning in fast mode during the ion beam milling. With this charge compensation approach, no sample drifting was detectable during the milling experiment, as monitored by SEM. To investigate the geometry of the newly milled pores, micrometer sized patterns were further milled adjacent to each pore to expose the cross sections of nanopores (Fig. 11c). The results were verified by SEM and presented in Fig. 11b and d. The designed tapered sidewall is confirmed after the geometry is exposed (Fig. 11d), and the proposed framework can be further used to tune the geometry for various potential uses.
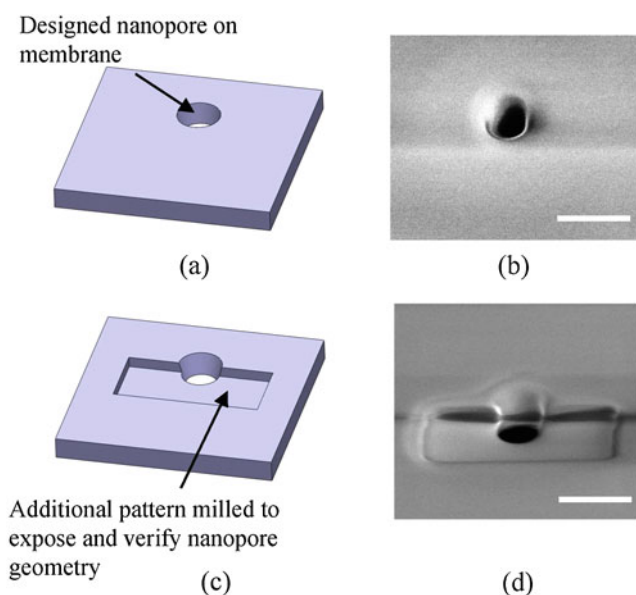
6 Conclusions

Charged particle beams, particularly FIB, are becoming flexible tools for fabrication and prototyping at the nano/microscale. However, a designed pattern to scan can contain millions of pixels, which results in an unprecedented large-scale problem for the process planning. A general framework of modeling and optimization for planning is proposed in this research, targeting arbitrary designed 3-D shapes. Enhanced with a number of optimization techniques, computational time and data storage requirement are effectively reduced. In addition, engineering aspects such as fabrication quality are also considered in the objective function. The proposed approach can be extended to machining processes, particular those at micro/nanoscale with the feature size approaching tool/beam size. The model formulation is also expected to enable FIB for scalable and automated applications. The optimization model proposed has built a scientific foundation for an immediate realization of complex yet more accurate and cost-effective, fabrication methods at micro/

Fig. 11 Schematic diagrams of **a** milling designed conical nanopore on 500-nm Si_3N_4 membrane and **c** exposing the nanopore geometry by milling additional cross section. The acquired SEM images are presented in **b** and **d** correspondingly (*scale bar* 1 μm)

nanoscale. For instance, the proposed planning approach can easily adopt the coarse-to-fine method; that is, a single object can be produced using multiple beam sizes with larger beams for faster material removal and smaller beams for greater geometry fidelity.

The optimization model has provided opportunities to streamline and promote FIB for flexible applications such as the two examples tested with submicron features. It should be noted that only simple examples were examined with predefined current settings. Results may require minor revision for complex geometries, e.g., high aspect ratio cavities. The results also motivate interesting thoughts that are worth of further studies. For instance, theoretical analysis may explain the actual physical phenomenon suggested by the roles of σ. This study has also built a foundation for using multiple beam sizes in producing a single 3-D shape, which will further improve the cost-effectiveness and fabrication quality of FIB milling. Numerical results suggest that a relative larger amount of errors were presented close to the boundaries of fabricated patterns; therefore, the error may be better controlled if the sparse level of fabrication is not uniform on the grid of pixels (e.g., less spacing at boundaries and areas with large curvature). The selections of starting points and termination conditions for the iterative algorithm also present opportunities for further improving the optimization scheme. All the points above require a formulation of repeated scanning and are subjects of future studies.

References

1. Reynjens S, Puers R (1999) A review of focused ion beam applications in microsystem technology. J Micromechanics Microengineering 11(4):287–300
2. Vasile MJ, Nassar R, Xie J, Guo H (1999) Microfabrication techniques using ion beams and emergent applications. Micron 30(3):235–244
3. Tseng AA (2004) Recent developments in micromilling using focused ion beam technology. J Micromechanics Microengineering 14(4):15–34
4. Tseng AA (2005) Recent developments in nanofabrication using focused ion beams. Small 1(10):924–939
5. Yao N, Wang Z (2005) Handbook of microscopy for nanotechnology. Kluwer Academic Pub., Norwell, MA
6. D'Souza RM, Sequin C, Wright PK (2004) Automated tool sequence selection for 3-axis machining of free-form pockets. J Comput Aided Des 36(7):595–605
7. Chen YH, Lee YS, Fang SC (1998) Optimal cutter selection and machining plane determination for process planning and NC machining of complex surfaces. J Manuf Syst 17(5):371–388
8. Xu XW, He Q (2004) Striving for a total integration of CAD, CAPP, CAM and CNC. Robot Comput-integr Manuf 20(2):101–109
9. Volkert CA, Minor AM (2007) Focused ion beam microscopy and micromachining. MRS Bull 32:389–395
10. Yong R (1993) Micro-machining using a focused ion beam. Vacuum 44(3–4):353–356
11. Vesile MJ, Niu Z, Nassar R, Zhang W, Liu S (1997) Focused iron beam milling: depth control for three dimensional microfabrication. J Vac Sci Technol B, Microelectron Nanometer Struct 15(6):2350–2354
12. Vasil MJ, Nassar R, Xie J (1999) Focused ion beam technology applied to microstructure fabrication. J Vac Sci Technol B, Microelectron Nanometer Struct 16(4):2499–2506
13. Fu Y, Bryan NKA, Shing ON, Hung NP (2000) Influence of the redeposition effect for focused iron beam 3D micromachining in silicon. Int J Adv Manuf Technol 16(12):877–880
14. Fu Y, Bryan NKA (2002) Semiconductor microlenses Fabricated by one-step-focused iron beam direct writing. IEEE Trans Semicond Manuf 15(2):229–231
15. Nassar R, Vasile MJ, Zhang W (1998) Mathematical modeling of focused ion beam microfabrication. J Vac Sci Technol B, Microelectron Nanometer Struct 16(1):109–115
16. Vasile MJ, Xie J, Nassar R (1999) Depth control of focused ion-beam milling from a numerical model of the sputter process. J Vac Sci Technol B, Microelectron Nanometer Struct 17(6):3085–3090
17. Fu Y, Bryan NKA, Shing ON, Wyan HNP (2000) Influence analysis of dwell time on focused ion beam micromachining in silicon. Sens Actuators 79(3):230–234
18. Adams DP, Vasile MJ (2006) Accurate focused ion beam sculpting of silicon using a variable pixel dwell time approach. J Vac Sci Technol B, Microelectron Nanometer Struct 24(2):836–844
19. Fu Y, Bryan NKA (2004) Fabrication of three-dimensional microstructures by two-dimensional slice by slice approaching via focused ion beam milling. J Vac Sci Technol, B, Microelectron Nanometer Struct 22(4):1672–1678
20. Hopman WCL, Ay F, Hu W, Gadgil VJ, Kuipers L, Pollnau M, de Ridder RM (2007) Focused ion beam scan routine, dwell time and dose optimizations for submicrometre period planar photonic crystal components and stamps in silicon. Nanotechnology 18(19):1–11
21. Tropp JA (2006) Just relax: convex programming methods for indentifying sparse signals in noise. IEEE Trans Inf Theory 52(3):1030–1051
22. Lee D, Seung S (2001) Algorithms for non-negative matrix factorization. Adv Neural Inf Process Syst 13:556–562
23. Sha F, Lin Y, Saul LK, Lee D (2007) Multiplicative updates for nonnegative quadratic programming. Neural Comput 19(8):2004–2031
24. Boyd S, Vandenberghe L (2004) Convex optimization. Cambridge University Press, New York, NY
25. Quanta (2009) 3D FEG 200/600 user operation manual, 7th edn. FEI Company, USA
26. http://www.srim.org/SRIM/SRIMLEGL.htm. Accessed 30 Sep 2011